A partial-dithering strategy for edge-illumination X-ray phase-contrast tomography enabled by a joint reconstruction method

Yujia Chen[1], Charlotte K. Hagen[2], Alessandro Olivo[2], Mark A. Anastasio[3]

[1]Washington University in St Louis, Department of Biomedical Engineering, Campus Box 1097, One Brookings Drive, St Louis, USA, 63130
[2]University College London, Department of Medical Physics and Biomedical Engineering, Malet Place, Gower Street, London WC1E 6BT, UK
[3]University of Illinois at Urbana-Champaign, Department of Bioengineering, 1102 Everitt Lab MC 278, 1406 W. Green St., Urbana, USA, 61801

E-mail: maa@illinois.edu

May 2019

Abstract. Edge-illumination X-ray phase-contrast tomography (EIXPCT) is a promising imaging technology where partially opaque masks are utilized with laboratory-based X-ray sources to estimate the distribution of the complex-valued refractive index. EIXPCT resolution is mainly determined by the period of a sample mask, but can be significantly improved by a dithering technique. Here, dithering means that multiple images per tomographic view angle are acquired as the object is moved over sub-pixel distances. Drawbacks of dithering include increased data-acquisition times and radiation doses. Motivated by the flexibility in data-acquisition designs enabled by a recently developed joint reconstruction (JR) method, a novel partial-dithering strategy for EIXPCT data-acquisition is proposed. In this strategy, dithering is implemented at only a subset of the tomographic view angles. The strategy can result in spatial resolution comparable to that of the conventional full-dithering strategy, where dithering is performed at every view angle, but the acquisition time is substantially decreased. Here, the effect of dithering parameters on image resolution are explored.

1. Introduction

X-ray phase-contrast tomography (XPCT) is a novel imaging technology utilized to estimate the complex-valued refractive index distribution of an object [**?**]. The complex-valued refractive index is denoted as $n = 1 - \delta + i\beta$, where δ denotes the refractive index decrement distribution and β denotes the absorption distribution. Compared with conventional computed tomography (CT) that estimates β only, XPCT takes advantage of the fact that, for many biological soft tissues, the contrast arising from δ is higher than that due to β. Variations in the object's refractive index decrement, δ, change

the phase of the X-ray wavefront when passing through the sample. Since the phase shift of the X-ray wavefront is not directly detectable, extra mechanisms are required to encode the phase shift information into detectable wave intensity changes. Depending on the encoding mechanism, XPCT can be classified into different types [**?**] that include propagation-based XPCT (PBXPCT) [**?**, **?**], grating-based XPCT (GBXPCT) [**?**, **?**], and edge-illumination XPCT (EIXPCT) [**?**, **?**, **?**, **?**]. EIXPCT, the focus of this article, is among a small group of XPCT technologies that have relatively weak requirements for source coherence, so they can be readily employed with laboratory-based X-ray sources [**?**, **?**]. Furthermore, the data-acquisition times in EIXPCT can be relatively short compared with other XPCT techniques that utilize laboratory-based sources [**?**].

The spatial resolution of the reconstructed EIXPCT images is influenced by several experimental factors that include the detector pitch, the mask period and the mask aperture size. If a higher resolution is desired, upgrading the entire hardware system is the most straight-forward solution. The upgrade requires reducing the period of the detectors and the masks. Moreover, a smaller source focal spot size is desired to prevent beamlets overlapping that obscures the images [**?**]. Although theoretically possible, in practice, the system upgrade is difficult to build due to its strict requirements, and can be extremely expensive even if it is possible. However, spatial resolution can also be improved by employing a data-acquisition strategy called dithering [**?**, **?**], without changing the detector, the masks, and the source. In this strategy, multiple images corresponding to different sub-pixel-translated object positions are acquired at a given tomographic view angle. These images can be interleaved together to form a single high-resolution image that corresponds to one that may have been acquired with a higher-resolution system. Ultimately, the reconstructed β and δ images will have enhanced spatial resolution as well.

Although the dithering technique boosts the spatial resolution of the reconstructed images, implementing dithering is time-consuming and thus hinders *in vivo* or radiation sensitive applications. In this study, motivated by the flexibility in data-acquisition designs enabled by a recently developed joint reconstruction (JR) method [**?**], a novel partial-dithering strategy is proposed. The core idea of partial-dithering is to implement dithering at only a subset of the tomographic view angles while obtaining no-dithering measurements at the rest of the view angles. The technique achieves a balance between image quality and data-acquisition time, improving image resolution over the no-dithering strategy and reducing the data-acquisition time over the full-dithering strategy.

2. Background

2.1. Imaging model

In EIXPCT imaging [**?**, **?**, **?**], phase information is obtained by employing a sample mask (or sample aperture), A_1, and a detector mask (or detector aperture), A_2, both of

which are shown in Figure 1(a). The object is placed immediately after A_1. When the relative positions of the two parallel masks are changed, different portions of the incident X-ray beam fall onto the sensitive areas of the detectors. Thus, the differential phase information is encoded in the X-ray wave intensity. EIXPCT imaging measures the wave intensity, from which the absorption and refractive index decrement distributions can both be estimated. The distance from the source to A_1 is denoted as l_{so}, and the distance between A_1 and A_2 is denoted as l_{od}. A_1 can be translated to achieve optimal phase contrast detectability. The displacement of the two masks after the translation is denoted by $\Delta\xi$. The imaged object can also be translated in the direction parallel to the masks over a distance of Δy. This movement is mainly used in the dithering step to be described in Sec.2.3, so Δy is referred to as the dithering offset.

A stationary coordinate system (x, y) is defined such that the x-axis is along the optical axis, and the y-axis is parallel to the two masks. During tomographic scanning, a rotation stage is set below the sample O. To describe the process, a rotated coordinate system (x_r, y_r) is attached to the stage. The origins of both coordinate systems overlap with the center of rotation for tomographic scan. The tomographic view angle measured from the positive x-axis is denoted as θ, and the two coordinate systems are related such that $x_r = x\cos\theta - y\sin\theta$, and $y_r = y\cos\theta + x\sin\theta$.

Let $\mathcal{H}_{\theta,y_r}$ denote the 2D Radon transformation:

$$\mathcal{H}_{\theta,y_r}(\beta(x,y)) = \int_{L(\theta,y_r)} \beta(x,y)dx_r, \tag{1}$$

where $L(\theta, y_r)$ denotes the line that goes through $(0, y_r)$ and is parallel to the x_r axis. Let $\mathcal{D}_{\theta,y_r}$ denote the first-order derivative of the 2D Radon transformation with respect to y_r:

$$\mathcal{D}_{\theta,y_r}(\delta(x,y)) = \frac{\partial}{\partial y_r}\int_{L(\theta,y_r)} \delta(x,y)dx_r. \tag{2}$$

The imaging process can thus be approximately described as [**?**, **?**]:

$$\begin{aligned} I(\theta, y_r, \Delta\xi, \Delta y) = \exp\left(-\frac{4\pi}{\lambda}\mathcal{H}_{\theta,y_r+\Delta y}(\beta(x,y))\right) \\ \cdot\left[I_{TC}(\Delta\xi) - \frac{l_{od}l_{so}}{l_{so}+l_{od}}I'_{TC}(\Delta\xi)\mathcal{D}_{\theta,y_r+\Delta y}(\delta(x,y))\right], \end{aligned} \tag{3}$$

where $I(\theta, y_r, \Delta\xi, \Delta y)$ is the normalized measured intensity at the tomographic view angle θ, detector pixel location y_r, mask-displacement $\Delta\xi$, and the object dithering offset Δy, and a measurement vector can be obtained by concatenating all measured data points. The wavelength of the monochromatic incident beam is denoted by λ. When polychromatic radiation is assumed, λ denotes the wavelength of the effective energy. The function $I_{TC}(\Delta\xi)$ describes the illumination curve that is acquired in a separate calibration procedure, which physically represents the intensity measured by a detector pixel when A_1 is translated along the y-axis in an air scan (i.e., without an

object). A typical illumination curve is shown in Figure 1(b). Let $I'_{TC}(\Delta\xi)$ denote the first-order derivative of the illumination curve.

In practice, the intensities are measured by discrete detectors. Suppose there are N_t samples of the intensity obtained during the entire data-acquisition process. Let $\boldsymbol{I}(\boldsymbol{\beta},\boldsymbol{\delta}) \in \mathbb{R}^{N_t}$ denote the vector concatenating all N_t intensity measurements generated from the estimate of the object's properties, where the k-th element of $\boldsymbol{I}(\boldsymbol{\beta},\boldsymbol{\delta})$ corresponds to the parameter combination $(\theta_k, y_{r(k)}, \Delta\xi_k, \Delta y_k)$. Thus,

$$\begin{aligned}[\boldsymbol{I}(\boldsymbol{\beta},\boldsymbol{\delta})]_k = \exp\left(-\frac{4\pi}{\lambda}\mathcal{H}_{\theta_k, y_{r(k)}+\Delta y_k}(\beta(x,y))\right) \\ \cdot\left[I_{TC}(\Delta\xi_k) - \frac{l_{od}l_{so}}{l_{so}+l_{od}} I'_{TC}(\Delta\xi_k)\mathcal{D}_{\theta_k, y_{r(k)}+\Delta y_k}(\delta(x,y))\right].\end{aligned} \tag{4}$$

The imaging model given in Eqn. (4) can be discretized for formulating the reconstruction problem as a finite-dimensional optimization problem. Let $\boldsymbol{\beta} \in \mathbb{R}^N$ denote the discretized absorption distribution where the elements in the vector are sampled values of absorption distribution at N vertices of a Cartesian grid. Similarly, $\boldsymbol{\delta} \in \mathbb{R}^N$ denotes the discretized refractive index decrement distribution. Let $\boldsymbol{H} \in \mathbb{R}^{N_t \times N}$ and $\boldsymbol{D} \in \mathbb{R}^{N_t \times N}$ denote the discretized version of the 2D Radon transform and its first-order derivative, respectively. The discretization of these operators is done by replacing the line integral of the continuous distribution β (or δ) along a beam trajectory by a weighted sum of all the elements in the discretized vector $\boldsymbol{\beta}$ (or $\boldsymbol{\delta}$), which is an approximation of the exact line integral: $\mathcal{H}_{\theta_k, y_{r(k)}+\Delta y_k}(\beta(x,y))$ is replaced by $[\boldsymbol{H}(\boldsymbol{\beta})]_k$; and $\mathcal{D}_{\theta_k, y_{r(k)}+\Delta y_k}(\delta(x,y))$ is replaced by $[\boldsymbol{D}(\boldsymbol{\delta})]_k$. Let $\boldsymbol{\Delta\xi} = [\Delta\xi_1, \Delta\xi_2, ..., \Delta\xi_{N_t}]^T \in \mathbb{R}^{N_t}$ be a collection of all the mask-displacements for all the N_t measurements. Then, the discretized imaging process can be written as:

$$[\boldsymbol{I}(\boldsymbol{\beta},\boldsymbol{\delta})]_k = \exp\left(-\frac{4\pi}{\lambda}[\boldsymbol{H}(\boldsymbol{\beta})]_k\right)\left(I_{TC}\left([\boldsymbol{\Delta\xi}]_k\right) - \frac{l_{od}l_{so}}{l_{so}+l_{od}} I'_{TC}\left([\boldsymbol{\Delta\xi}]_k\right)[\boldsymbol{D}(\boldsymbol{\delta})]_k\right). \tag{5}$$

During the data-acquisition process, the view angle θ, detector pixel location y_r, mask-displacement $\Delta\xi$, and the object dithering offset Δy can all be varied. For each X-ray exposure, the view angle θ, mask-displacement $\Delta\xi$ and dithering offset Δy are all fixed. The R different detector elements in the detector collect measurement data at R different detector pixel locations, $y_{r(j)}$ $(j = 1, 2, ..., R)$. A typical tomographic dataset acquires images at V different view angles θ_i $(i \in \{1, 2, ..., V\})$, equally distributed over a 2π scanning angular range. The data-acquisition design for a tomographic scan entails determining the choice of the $\Delta\xi$ and Δy values at each exposure, which also determines the number of exposures at each view angle.

2.2. Mask-displacement selection strategy and joint reconstruction method

The illumination curve informs selection of the mask-displacement, $\Delta\xi$. Figure 1(b) shows a typical illumination curve, I_{TC}, as introduced in Eqn. (4). Given Eqn. (4), the

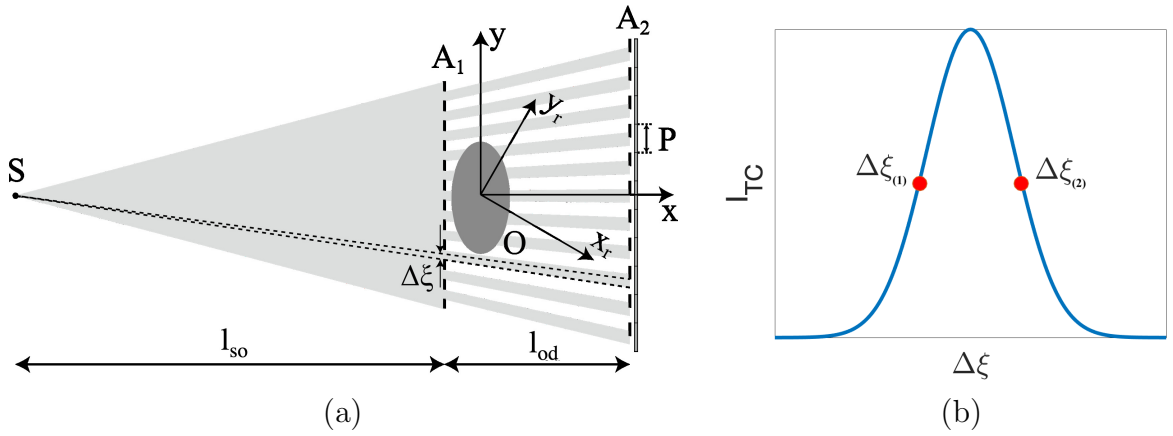

Figure 1. (a) Illustration of the EIXPCT system. (b) A typical illumination curve. The exposures are usually acquired at the two marked locations corresponding to half-maximum illumination level.

most efficient way to maximize the δ-signal contrast in the measured intensity signals is to adjust the mask to a special location where the derivative of the illumination curve is largest. The two half-maximum locations, $\Delta\xi_{(1)}$ and $\Delta\xi_{(2)}$, both satisfy this condition, as shown in Figure 1(b).

A mask-displacement strategy selects one of these two locations. The selection of $\Delta\xi$ is closely related to the reconstruction method employed. The measurement data should be acquired so that the reconstruction algorithm is capable of accurately and stably estimating for the absorption and refractive index decrement distributions. The conventional reconstruction method employs a two-step approach [**?**] – a phase-retrieval step followed by a tomographic reconstruction step. It requires taking exposures at both mask-displacements at each tomographic view angle.

A recently proposed joint reconstruction (JR) method that combines the phase-retrieval step with the tomographic reconstruction step can enable different mask-displacement strategies. The JR method seeks to estimate the $\boldsymbol{\beta}$ and $\boldsymbol{\delta}$ distributions of the object by solving an optimization problem [**?**]:

$$(\tilde{\boldsymbol{\beta}}, \tilde{\boldsymbol{\delta}}) = \arg \min_{\boldsymbol{\beta}\geq 0, \boldsymbol{\delta}\geq 0} f(\boldsymbol{\beta}, \boldsymbol{\delta}) = \arg \min_{\boldsymbol{\beta}\geq 0, \boldsymbol{\delta}\geq 0} ||\mathbf{I}_m - \mathbf{I}(\boldsymbol{\beta}, \boldsymbol{\delta})||^2 + R(\boldsymbol{\beta}, \boldsymbol{\delta}), \qquad (6)$$

where $R(\boldsymbol{\beta}, \boldsymbol{\delta})$ is a penalty term. Here, the acquired measurement vector $\mathbf{I}_m$ is the concatenation of all measured intensities, and $\mathbf{I}(\boldsymbol{\beta}, \boldsymbol{\delta})$ is the simulated measurement vector which is the concatenation of the intensity measurements based on Eqn. (4) considering the current estimate of the object's absorption distribution, $\boldsymbol{\beta}$, and refractive index decrement distribution, $\boldsymbol{\delta}$. It has been proven that the JR method requires taking exposures at only one mask-displacement at each view angle. Also, selecting which mask-displacement to use at each view angle can be flexible, and the selection strategy has been extensively discussed in previous works [**?**, **?**].

In this work, the focus is on the dithering strategies for selecting Δy. One typical data-acquisition design is investigated as an example – the Alternating Aperture Position

plan covering an angular range of 2π (abbreviated as the AAP (2π) plan) as introduced previously [**?**]. With this design, the object is imaged at V tomographic view angles uniformly distributed over a 2π range: $\theta_i = 2\pi(i-1)/N$ $(i = 1, 2, ..., V)$. At each tomographic view angle θ_i, one mask-displacement, $\Delta\xi_i$, is selected from two optimal locations that correspond to maximum absolute gradients of the illumination curve. The displacement is $\Delta\xi_{(1)}$ for odd views, and $\Delta\xi_{(2)}$ for even views. The following discussion assumes the AAP (2π) design is employed.

2.3. Dithering technique

Dithering is the process of moving the object over sub-pixel distances and obtaining multiple images to artificially increase resolution [**?**]. Dithering can be incorporated in any data-acquisition design using any mask-displacement selection strategy. If K-step dithering is employed, K times as many exposures are required compared to the no-dithering situation. In a K-step dithering strategy, K images are acquired at dithering offsets

$$\Delta y_k = \frac{k-1}{K}\frac{l_{so}}{l_{so}+l_{od}}P, (k = 1, 2, ..., K). \tag{7}$$

The K images are later stitched together to form an image sampled at a finer pitch. If tomography is performed, a high resolution reconstructed image can be obtained from the resolution-enhanced acquired data, but at the cost of $K-1$ extra exposures per tomographic view angle.

3. Methods

A novel dithering strategy for EIXPCT called partial-dithering is proposed. For clarity of notation, the conventional dithering technique will be called full-dithering.

3.1. No-dithering, full-dithering, and partial-dithering

When there is no dithering employed, one exposure is acquired at each tomographic view angle: R detector elements collect R measured intensities at locations y_{rj} $(j = 1, 2, ..., R)$ with $\Delta y = 0$. The intensities $I(\theta_i, y_{rj}, \Delta\xi_i, \Delta y = 0)$ are measured for $i \in \{1, 2, ..., V\}$ and $j \in \{1, 2, ..., R\}$.

When K-step full-dithering is employed, at every view angle, K images are acquired, corresponding to $\Delta y = (k-1)P/K$ $(k = 1, 2, ..., K)$, where P is the period of the sample mask, A_1. In this situation, $I(\theta_i, y_{rj}, \Delta\xi_i, \Delta y_k)$ is measured for $i \in \{1, 2, ..., V\}$, $j \in \{1, 2, ..., R\}$, and $k \in \{1, 2, ..., K\}$.

In the novel partial-dithering strategy proposed in this work, instead of implementing dithering at every view angle, dithered measurement data are acquired only at every D views, and thus there are V/D dithering views as well as $V - V/D$ non-dithered views. D is defined as the dithering interval. To simplify the discussion, V/D is assumed to be an integer in this work. The dithered view set is defined as

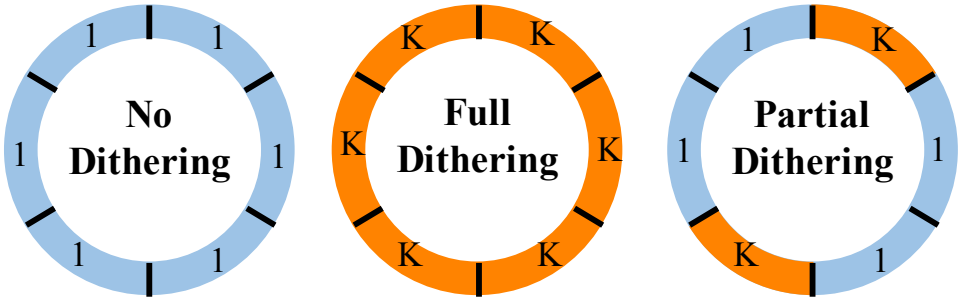

Figure 2. A comparison between no-dithering, full-dithering and partial-dithering when $V = 6$ and $D = 3$. Each arc represents a tomographic view angle. The numbers on the arcs denote the number of exposures taken at the view angle. The orange arc means K-step dithering is implemented at the view angle, while a blue arc means there is only 1 exposure taken.

$S_d = \{1, D+1, 2D+1, ..., V-D+1\}$, and the complementary non-dithered view set is defined as $S_n = \{1, 2, ..., V\} \setminus S_d$. Consequently, $I(\theta_i, y_{rj}, \Delta\xi_i, 0)$ is measured for $i \in S_n$, $j = 1, 2, ..., R$, and $I(\theta_i, y_{rj}, \Delta\xi_i, \Delta y_k)$ is measured for $i \in S_d$, $j \in \{1, 2, ..., R\}$, and $k \in \{1, 2, ..., K\}$. Figure 2 illustrates no-dithering, full-dithering, and partial-dithering. For an object with an absorption distribution $\boldsymbol{\beta}$ and refractive index decrement distribution $\boldsymbol{\delta}$, concatenating the measured intensities from all dithering views yields the dithered measurement vector, $\mathbf{I}_d(\boldsymbol{\beta}, \boldsymbol{\delta})$, and concatenating those from non-dithering views yields the non-dithered measurement vector, $\mathbf{I}_n(\boldsymbol{\beta}, \boldsymbol{\delta})$. The total data-acquisition time is proportional to the number of exposures required during the data-acquisition process. For each combination of θ_i and Δy_k, one exposure is required. Thus the total number of required exposures is equal to the total number of $(\theta_i, \Delta y_k)$ combinations, which is $V + (V/D) \cdot (K-1)$. Figure 3 depicts the number of exposures required for various dithering intervals. Merely increasing D from 1 to 2 can almost reduce the data-acquisition time by one-half.

3.2. Image reconstruction from partial-dithered measurement data

Conventional analytic two-step reconstruction methods for EIXPCT [**?**] are suboptimal for use with acquired images whose spatial resolution varies with view angle, such as produced with the partial-dithering strategy. To circumvent this, a modified version of the JR method is employed to reconstruct image estimates from measured intensity data that are dithered at only a subset of view angles. A modified cost function is defined as a weighted least squares data fidelity term with a total variation (TV) penalty term:

$$f = \alpha_n \|\mathbf{I}_{m,n} - \mathbf{I}_n(\boldsymbol{\beta}, \boldsymbol{\delta})\|^2 + \alpha_d \|\mathbf{I}_{m,d} - \mathbf{I}_d(\boldsymbol{\beta}, \boldsymbol{\delta})\|^2 + R(\boldsymbol{\beta}, \boldsymbol{\delta}), \tag{8}$$

where $\mathbf{I}_{m,n}$ and $\mathbf{I}_{m,d}$ denote the experimentally acquired measured intensities in all non-dithering and dithering views, respectively, and $R(\boldsymbol{\beta}, \boldsymbol{\delta})$ is the weighted TV penalty of $\boldsymbol{\beta}$ and $\boldsymbol{\delta}$. Here, α_n and α_d are the weights of non-dithering and dithering views in the data fidelity term.

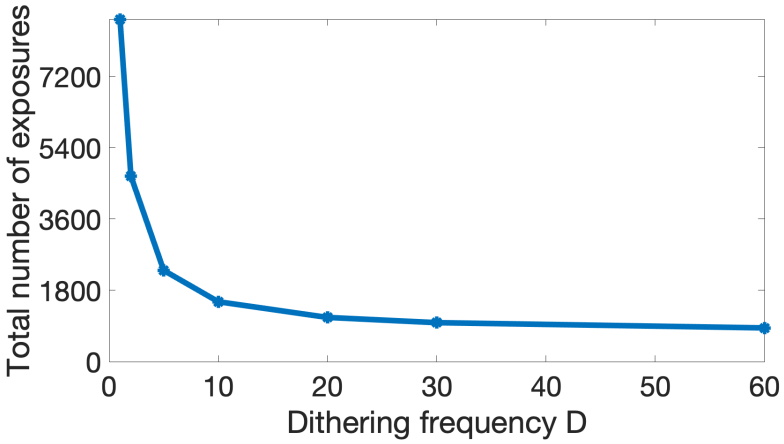

Figure 3. A demonstration of the time-saving effect of the partial-dithering strategy. It shows the total number of X-ray exposures for 12-step ($K = 12$) partial-dithering acquisition with 720 view angles as a function of dithering interval D, which is a feasible setup in experiments. The marked data points correspond to $D = 1, 2, 5, 10, 20, 30,$ and 60. The number of exposures is proportional to the data-acquisition time. Merely increasing D from 1 to 2 can reduce the required number of exposures from 8640 to 4680, with a corresponding 46% reduction in the data-acquisition time.

The weights α_n and α_d can be tuned to achieve the desired reconstructed image quality. In general, increasing α_n puts more emphasis on the contribution from non-dithered measurement data; this approach yields faster solution convergence but lower image resolution. On the contrary, increasing α_d is expected to improve image quality, but has the disadvantage of slower algorithm convergence. To combine the merits of both approaches, a two-phase iterative reconstruction is proposed. In the first phase, the value of α_n is high but the value of α_d is low, so a low-resolution converged solution can be obtained quickly, and the result can serve as the initial guess for the second phase. In the second phase, the value of α_n is low but the value of α_d is high, so the details can be better refined. The exact values of α_n and α_d are tuned empirically.

3.3. Simulation studies

The 2-dimensional (2D) geometric phantom shown in Figure 4 was employed in the computer-simulation studies. The elements within the phantom include a small ellipse, a bar, and a triangle region with converging bars. The phantom assumes adipose tissue as the material for the big ellipse and soft tissue as that for the small ellipse, the bar, and the triangles [**?**]. The δ and β values for the adipose tissue are 3.807×10^{-7} and 6.499×10^{-11}, respectively. Those for soft tissue are 4.204×10^{-7} and 1.320×10^{-10}, respectively.The triangle region at the top is designed for analysis of resolution. All 6 of the small triangular bars are 200 μm in base and 4 mm in height. The bases of all the small triangular bars are aligned vertically, and the distance between the bases of neighboring triangular bars is also 200 μm. A vertical line, denoted as a scan line, can

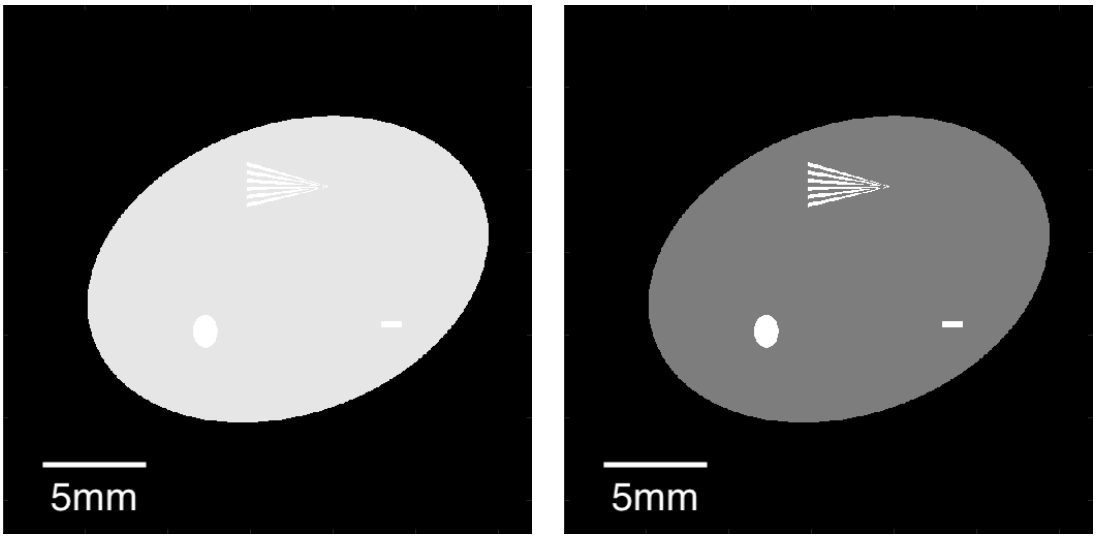

Figure 4. The refractive index decrement distribution phantom (left) and the absorption distribution phantom (right).

be moved from the left to the right in the triangle region. The profile extracted from the scan line contains periodic patterns that are equivalent to profiles obtained for periodic bars. When profiles are obtained at different horizontal locations, the bar gap width will change from 200 μm to 0 μm. In order to analyze the system's resolution, the scan line is moved from left to right until the periodic patterns can no longer be resolved in the profile. In this way, the triangle pattern can provide insights about the resolution of the reconstructed images.

An X-ray parallel beam with the effective energy of 24 keV was assumed to irradiate the object. The two masks were positioned so that $l_{so} = 1.6\,\mathrm{m}$ and $l_{od} = 0.4\,\mathrm{m}$. Simulated measurement data were obtained from 720 tomographic views that were evenly distributed over 360 degrees. The detector contained a row of 400 pixels with a pixel size of $100\,\mu$m. Five-step dithering was implemented every D views. Dithering was performed with $\Delta y = 20\,\mu$m. Several different dithering intervals were tested: $D = 1, 2, 5, 10, 20, 30$, and 60, with $D = 1$ representing the full-dithering situation. A no-dithering situation was also included for comparison. The measurement data were simulated based on Eqn. (4), with an analytical integration step in the Radon transformation and Poisson noise added. The illumination curve was modeled after a previous experiment [**?**]. At the optimal mask-displacements, $\Delta\xi_1 = -8\,\mu$m and $\Delta\xi_2 = 8\,\mu$m, the values of I_{TC} and the corresponding gradient I'_{TC} can be read from the illumination curve as $I_{TC1} = I_{TC2} = 0.5$ a.u. (arbitrary unit), and $I'_{TC1} = 4 \times 10^4\,\mathrm{m}^{-1}$, $I'_{TC2} = -4 \times 10^4\,\mathrm{m}^{-1}$. The phantom was reconstructed with a $2\,\mu$m pixel size. During the two-phase reconstruction, $\alpha_n = 1, \alpha_d = 0$ were selected for the first phase, and $\alpha_n = 0.1, \alpha_d = 1$ were selected for the second phase. To make sure the reconstructions at different dithering intervals received similar levels of TV regularization, the weight for the TV penalty was chosen to be proportional to the total number of measured data

points. The fast iterative shrinkage-thresholding algorithm (FISTA) [**?**] was employed to minimize the cost defined in Eqn. (8). The iteration loop stops when the cost is below a certain threshold selected by trial and error.

3.4. Experimental validation

Experimental data acquired in a previous study [**?**] were employed to validate the feasibility of the proposed data-acquisition designs. The imaged object was a custom-built phantom consisting of a hollow plastic cylinder, a plastic rod, a smaller hollow plastic cylinder, rolled plastic paraffin film, and chalk inside a plastic container. Additional details of the imaging system and parameters can be found in the quoted study [**?**]. The rolled plastic paraffin film region contains many fine structures, which are used as the focus of our resolution analysis. In the partial-dithering strategy, several different D values were tested: $1, 2, 5, 10, 20, 30$, and 60. At the dithering views, a ten-step sub-pixel dithering ($K = 10$) of the imaged object was employed. During the two-phase reconstruction, α_n and α_d were set as 1 for the first phase, and $\alpha_n = 0, \alpha_d = 1$ were selected for the second phase. The weight for the TV penalty was also chosen to be proportional to the total number of measured data points. The pixel size of the reconstructed images was 8.8 μm.

4. Results

4.1. Computer-simulation studies

The reconstructed estimates of $\boldsymbol{\delta}$ with different dithering intervals are shown in Figure 5(a) and a zoomed-in view of the triangle regions are shown in Figure 5(b). The boundaries of the triangular bars become clearer with increasing numbers of dithering views. The gaps between neighboring triangular bars shrink from left to right. When the number of dithering views increases, smaller gaps begin to be differentiated. The differentiation can be better shown in Figure 7, where the reconstructed profiles and the ground truth profiles are compared at different dithering intervals. The profiles are obtained from the same vertical scan line, along which the neighboring triangular bars have a gap of 80 μm. At this location, only the reconstructed profiles of D=1 and D=2 can unambiguously show the differentiation. The others are unable to reveal the pattern details.

For a more quantitative analysis, we have calculated the root mean square error (RMSE), the contrast to noise ratio (CNR), and the structural similarity (SSIM) [**?**] as metrics for reconstruction quality evaluation. The RMSE is the root of mean square error of every pixel and thus describes the noise level in the reconstructed image. A smaller RMSE indicates less noisy reconstruction. The CNR is defined as the ratio between contrast and the RMSE, where the contrast is the difference of theoretical values between adipose tissue and soft tissue. A higher CNR is considered better for differentiating different structures. The SSIM between the reconstructed image and the

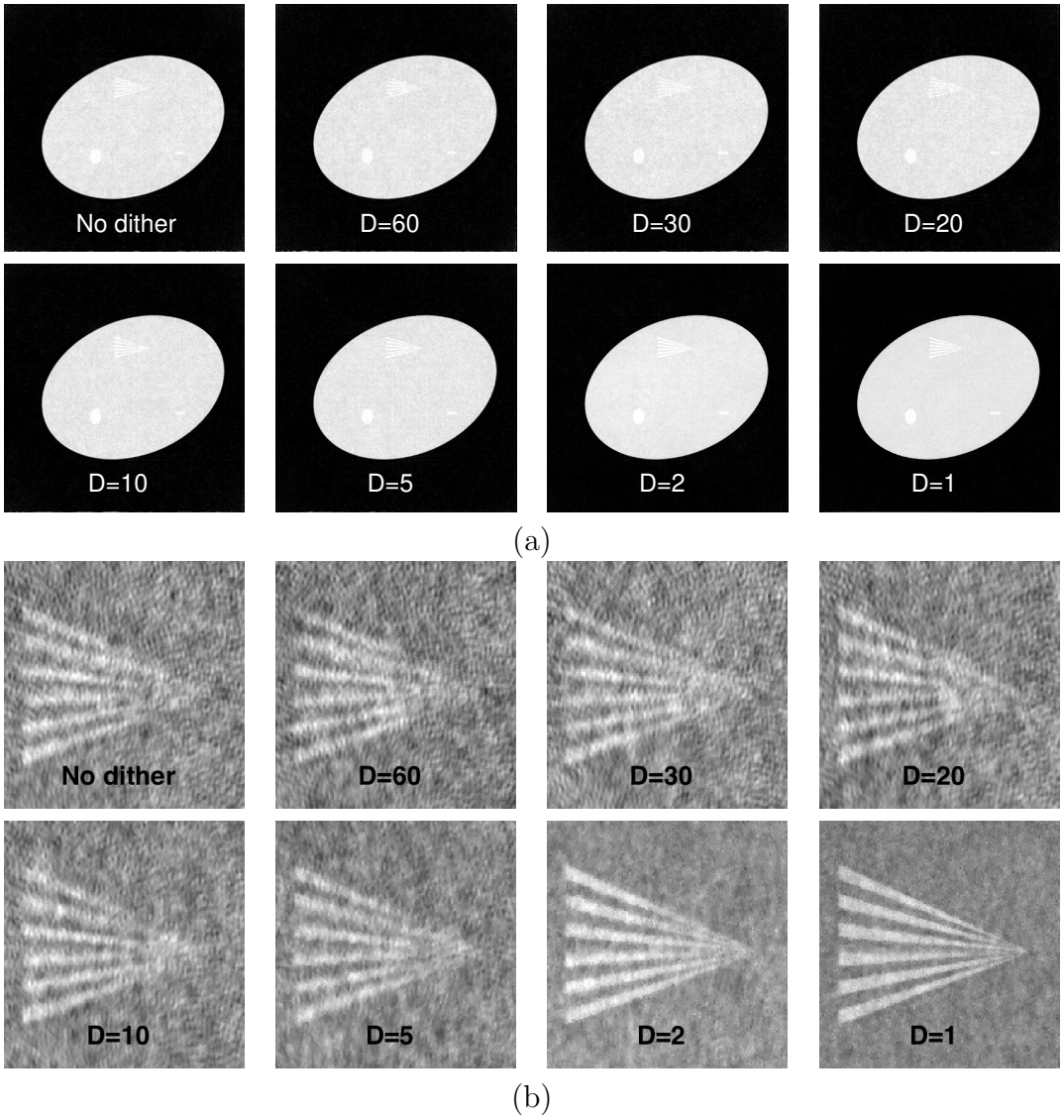

Figure 5. (a) The reconstructed refractive index decrement distributions when the interval of dithering changes. (b) The triangle regions of the reconstructed refractive index decrement distributions when the interval of dithering changes (grayscale adjusted to enhance the visual contrast of the triangle patterns). When dithering is implemented more frequently, it is easier to differentiate the triangular bars, indicating that the resolution increases.

ground truth image better describes the perceptual structure resemblance. The SSIM value varies between 0 and 1 and a value closer to 1 indicates higher resemblance. These metrics as a function of dithering interval are given in Figure 6. The charts reveal that the quality is better when dithering is implemented more frequently. When the dithering interval is too large, the reconstructed image quality is similar to that without dithering and thus the benefit is negligible.

To further analyze the resolution improvement, the peak-gap-ratio (PGR) is introduced. For each profile extracted at one particular vertical scan line in the triangle

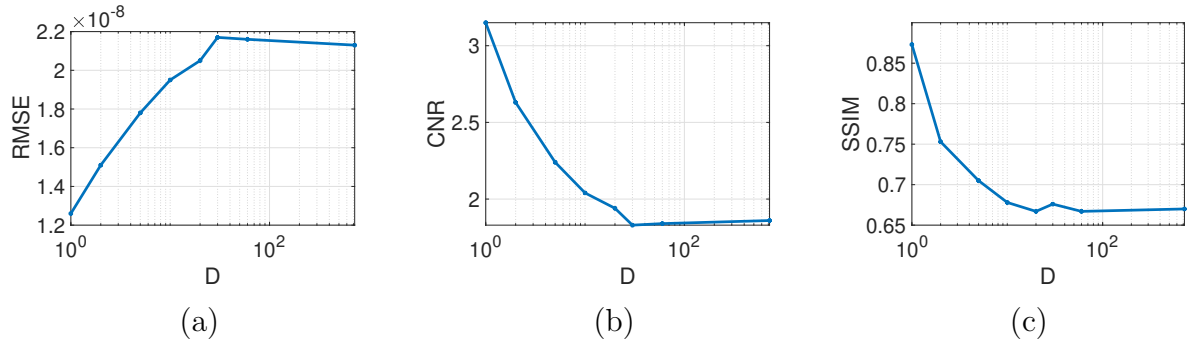

Figure 6. The relationships between the (a) RMSE (b) CNR (c) SSIM values and the dithering interval D. When D is smaller than 30, more frequent dithering leads to larger CNR, larger SSIM and smaller RMSE, all of which indicate higher image quality in general. When D is over 30, none of the metrics vary significantly with D varying, and the fluctuations in quality metrics are mainly due to noise.

region of the reconstructed image, the values of all the reconstructed pixels within the triangular bars, highlighted in red in Figure 8(a), were averaged and a peak value was obtained; then, the values of all the reconstructed pixels in the gap region between triangular bars, highlighted in blue in Figure 8(a), were averaged and a gap value was obtained. The ratio of the peak value to the gap value is defined as the PGR. When two peaks are separated clearly, the peak region is significantly higher than the gap region so PGR is large. When two peaks are blurred out and undistinguishable, the peak and gap regions will share similar values so the PGR will be close to 1. In summary, a larger PGR indicates better differentiability.

A illustration of the PGR values as a function of dithering interval and gap size is shown in Figure 8(b), and a thresholded version is given in Figure 8(c). The ground truth PGR is approximately 1.1 in this test set. Figure 8(b) and Figure 8(c) both show that when dithering is more frequent, the PGR can maintain a relatively high value for a much smaller gap size, providing a quantitative estimate of the degree to which that partial-dithering can help improve resolution.

4.2. Experimental validation

The rolled plastic paraffin film regions of the estimates of $\boldsymbol{\delta}$ reconstructed from the experimentally acquired data are shown in Figure 9. Zoomed-in views of a small region (the bottom left corner of the rolled plastic paraffin film region) are shown in Figure 10. The separation of two closely located films, with a gap of approximately 12 μm, becomes clearer with more dithering views. The two films are clearly separated for $D \leq 5$. This trend indicates that better resolution can be obtained when D is smaller. Note that the artifacts in the no-dithering reconstructed image are related to the loss of reliability of the retrieved phase shift values caused by under-sampling [**?**]. Similar to the full-dithering strategy, partial-dithering also suppresses these artifacts by increasing the sampling rate at the dithered views.

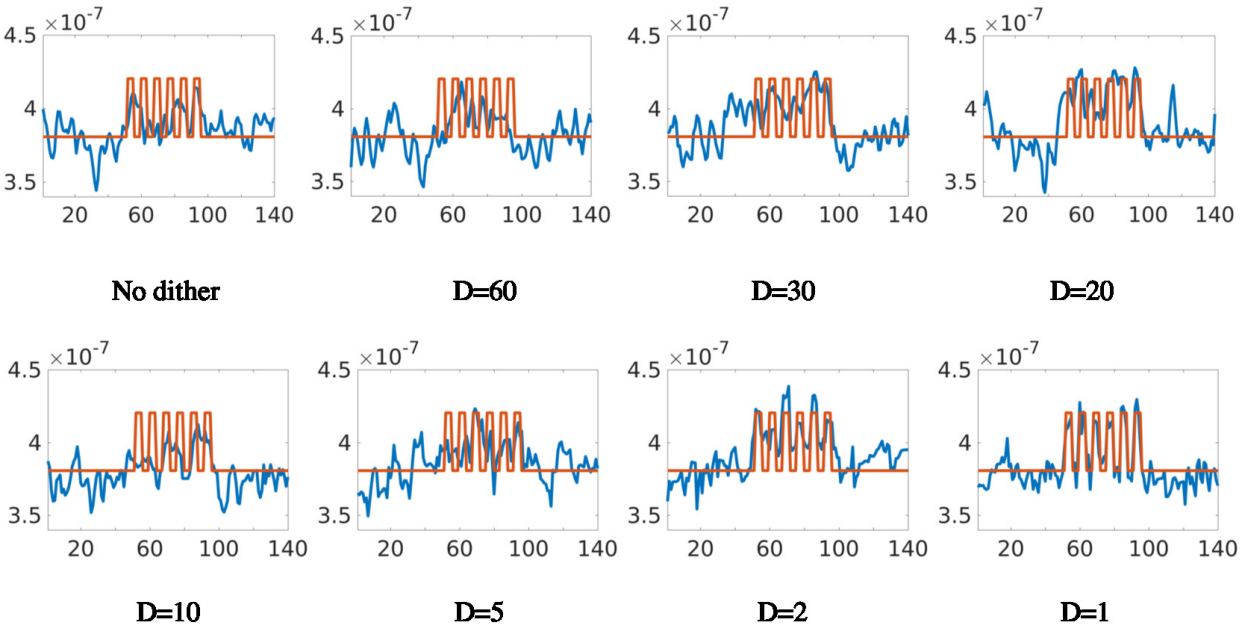

Figure 7. The profiles of the actual refractive index decrement distribution (red) and reconstructed refractive index decrement distribution (blue) along one vertical line in the triangle region when the interval of dithering changes. The gaps between the triangular bars at this profile are all 80μm. The different structures are most clearly separated when the dithering interval is 1 or 2. The other reconstructed profiles are dominated by noise and fail to show strong periodic patterns.

5. Conclusion

To enhance spatial resolution in EIXPCT, dithering can be employed. This technique moves the to-be-imaged object by a series of sub-pixel distances and acquires measurement data at the different dithering locations. The images acquired at each X-ray exposure are later combined into a higher-resolution image, from which an enhanced resolution reconstructed tomographic image can be computed. The main drawbacks of the dithering technique are prolonged data-acquisition times and increased radiation doses. In this article, a partial-dithering strategy was proposed for EIXPCT where dithering is applied periodically at a subset of tomographic view angles at which data were acquired. Compared with the conventional full-dithering technique, partial-dithering greatly reduces the data-acquisition time, but improves spatial resolution over the no-dithering case.

Image reconstruction from partially-dithered measurement data was enabled by the use of an iterative joint reconstruction (JR) method, which was implemented in two steps to improve reconstruction speed. The non-dithered views were weighted more heavily in the first JR phase so that a low-resolution converged solution can be quickly obtained. The dithered views were weighted more heavily in the second JR phase to maximize the spatial resolution improvement. It was demonstrated that, with partial-dithering,

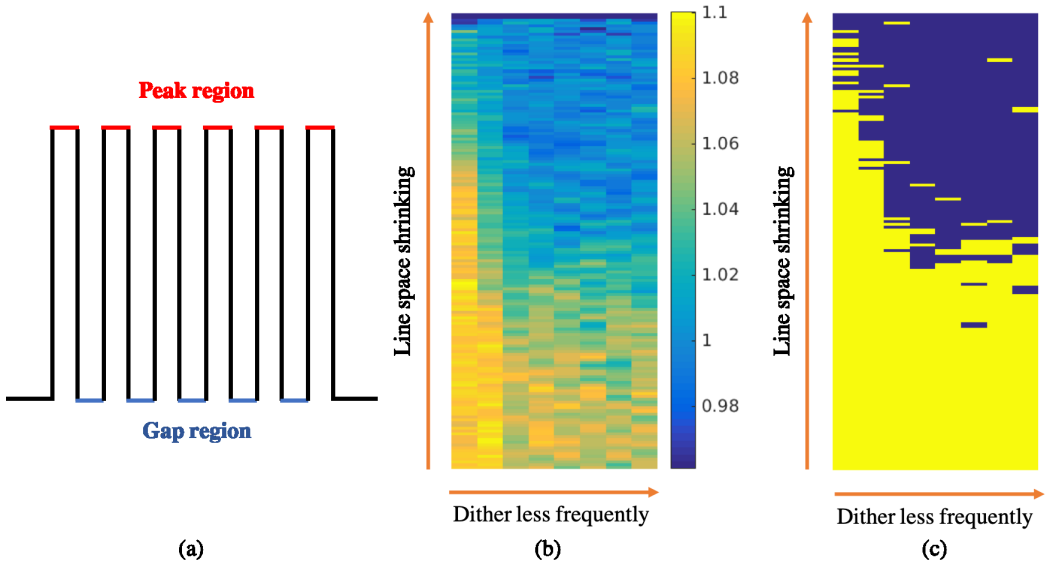

Figure 8. (a) Illustration of the peak region and the gap region. The entire line represents a typical line profile along one vertical line in the triangle region in the phantom. The red pixels represent the peak region and the blue pixels represent the gap region. (b) The PGRs calculated for the refractive index decrement distributions at different vertical lines, corresponding to different gaps between the triangle patterns. The horizontal direction corresponds to 8 different dithering intervals: 1, 2, 5, 10, 20, 30, 60, and no dither. For the same gap between triangle patterns, when dithering is implemented more frequently, the PGR is in general larger. (c) A thresholded PGR image. The yellow regions correspond to ratios larger than an empirically selected threshold of 1.02. Other thresholds may be selected depending on the application but the conclusion remains unchanged: more frequent dithering helps differentiating periodic structures at a finer resolution.

the image resolution was improved compared with no-dithering, and the data-acquisition time is shorter than that of full-dithering. Partial-dithering is a first exploration of novel dithering strategies, and more flexible dithering strategies can be studied in the future. Moreover, the dithering strategy can also be combined with mask-displacement selection strategy [**?**]. Such creative designs could potentially provide better reconstructed image quality, with even shorter data-acquisition times.

ACKNOWLEDGMENTS

This work was supported in part by NIH award EB020604, EPSRC grants EP/L001381/1 and EP/I021884/1. CKH is supported by the Royal Academy of Engineering under the RAEng Research Fellowship scheme.

References

[1] Momose A 2005 *Japanese Journal of Applied Physics* **44** 6355

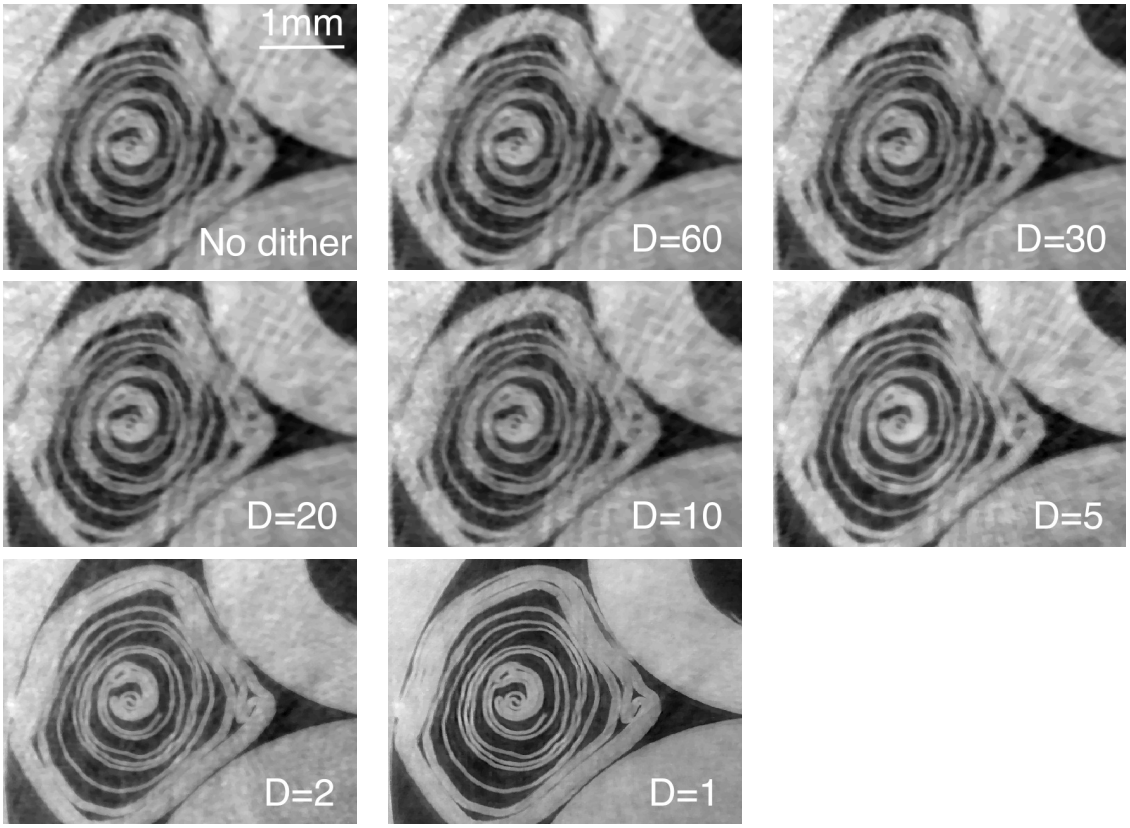

Figure 9. The rolled plastic paraffin film regions of the reconstructed refractive index decrement distributions when the interval of dithering changes. When the dithering interval is lower, the resolution improves and artifacts are diminished.

[2] Diemoz P, Bravin A and Coan P 2012 *Optics express* **20** 2789–2805
[3] Wilkins S, Gureyev T E, Gao D, Pogany A and Stevenson A 1996 *Nature* **384** 335
[4] Paganin D and Nugent K A 1998 *Physical review letters* **80** 2586
[5] Pfeiffer F, Weitkamp T, Bunk O and David C 2006 *Nature physics* **2** 258
[6] Kottler C, Pfeiffer F, Bunk O, Grünzweig C and David C 2007 *Review of scientific instruments* **78** 043710
[7] Munro P R, Hagen C K, Szafraniec M B and Olivo A 2013 *Optics express* **21** 11187–11201
[8] Olivo A and Speller R 2007 *Applied Physics Letters* **91** 074106
[9] Olivo A and Speller R D 2008 A novel x-ray imaging technique based on coded apertures making phase contrast imaging feasible with conventional sources *Nuclear Science Symposium Conference Record, 2008. NSS'08. IEEE* (IEEE) pp 1447–1450
[10] Hagen C, Diemoz P, Endrizzi M, Rigon L, Dreossi D, Arfelli F, Lopez F, Longo R and Olivo A 2014 *Optics express* **22** 7989–8000
[11] Zamir A, Hagen C, Diemoz P C, Endrizzi M, Vittoria F, Chen Y, Anastasio M A and Olivo A 2017 *Journal of Medical Imaging* **4** 040901
[12] Diemoz P C, Vittoria F A and Olivo A 2014 *Optics express* **22** 15514–15529
[13] Hagen C, Munro P, Endrizzi M, Diemoz P and Olivo A 2014 *Medical physics* **41**
[14] Hagen C, Diemoz P, Endrizzi M and Olivo A 2014 *Journal of Physics D: Applied Physics* **47** 455401
[15] Chen Y, Guan H, Hagen C K, Olivo A and Anastasio M A 2017 *Optics Letters* **42** 619–622
[16] Olivo A and Speller R 2008 *Physics in medicine and biology* **53** 6461

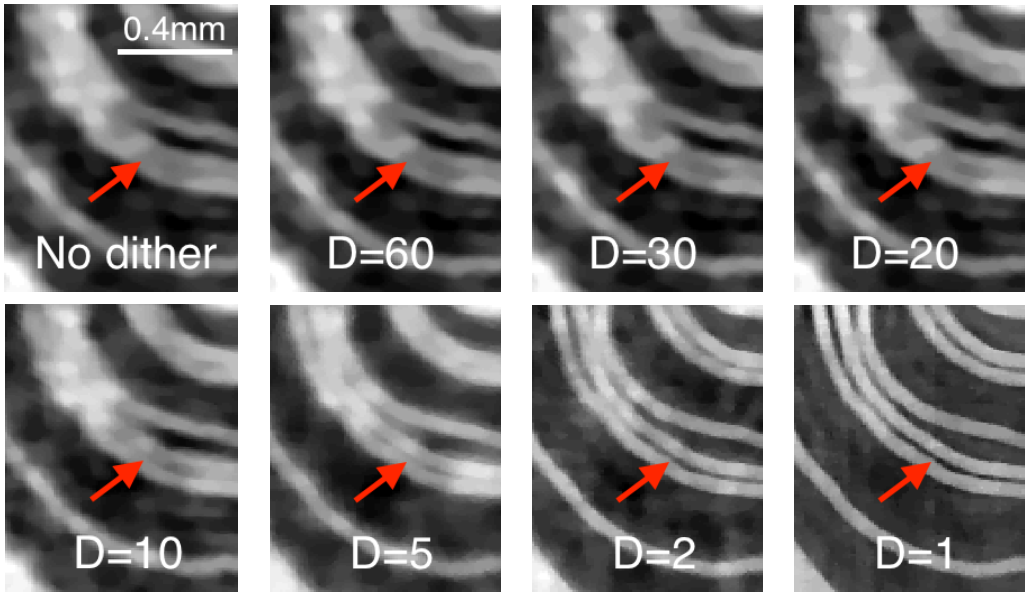

Figure 10. Zoomed-in views of the bottom left corner in the rolled plastic paraffin film region of the reconstructed refractive index decrement distributions when the interval of dithering changes. When the dithering interval is lower, the separation between two close films becomes clearer.

[17] Chen Y, Zhou W and Anastasio M A 2018 Joint-reconstruction-enabled data acquisition design for single-shot edge-illumination x-ray phase-contrast tomography *Medical Imaging 2018: Physics of Medical Imaging* vol 10573 (International Society for Optics and Photonics) p 1057322

[18] Henke B, Gullikson E and Davis J 1993 Atomic data and nuclear data tables vol. 54

[19] Diemoz P, Hagen C, Endrizzi M, Minuti M, Bellazzini R, Urbani L, De Coppi P and Olivo A 2017 *Physical Review Applied* **7** 044029

[20] Wang Z, Bovik A C, Sheikh H R, Simoncelli E P *et al.* 2004 *IEEE transactions on image processing* **13** 600–612